Dynamics of plasma vortices: The role of the electron skin depth

Dynamics of plasma vortices: The role of the electron skin depth

J. H. Mentink, J. Bergmans,[a] L. P. J. Kamp, and T. J. Schep
Department of Applied Physics, Technical University of Eindhoven, P.O. Box 513, NL-5600 MB Eindhoven, The Netherlands

(Received 18 February 2005; accepted 8 March 2005; published online 2 May 2005)

The drift-Alfvén equations for a quasineutral plasma that is permeated by a strong background magnetic field describe the plasma dynamics in the transverse plane. Three scalar fields—which are linear combinations of parallel current, fluid vorticity, and density—are incompressibly advected by three streaming potentials. These three "generalized vorticities" are point-wise conserved. Their dynamics is studied numerically using the method of Contour Dynamics, which for this purpose is generalized from one to three different types of vorticity. In the regime where the electron inertial skin depth d_e is smaller than the ion sound gyroradius, the interaction dynamics of patches of generalized vorticity shows a preference for the formation of structures with length scale $O(d_e)$. In this regime quasiperiodic splitting-merging cycles of single vorticity patches occur. These vortex interactions are considered to be the paradigm for the interactions of separated vortical structures in a strongly magnetized turbulent plasma. © *2005 American Institute of Physics*. [DOI: 10.1063/1.1900003]

I. INTRODUCTION

In the study of fluids and turbulent plasmas one frequently considers the interaction between long-lived coherent structures. We will loosely call such structures *vortices*. These coherent structures resemble localized and stationary solutions of the fluid equations. When they are relatively far apart their relative motion may be described by a point-vortex model.[1,2] When the motion of the fluid brings the vortices at close distances of each other the spatial extent and shape of the vortices become important. "Inelastic collisions" take place on a relatively fast time scale. After the interaction process a new state emerges consisting of one or more vortices which, in their further motion, might again be tracked using the point-vortex approximation. Examples of vortex collisions are the merging of like-sign vortices[3] and the destruction of a vortex in a three vortex interaction called the vortex collapse.[4,5]

In Refs. 3,4 these interactions are analyzed by considering that the vortices are *finite-area-vortex-regions* (FAVRs). These are regions in the fluid where the vorticity is constant and uniform, bounded by a deformable contour. The motion of such piecewise constant vorticity distributions can be described consistently by the dynamics of the contours. This essentially reduces the dimensionality of the problem. The method of describing the motion of FAVRs by the advection of their boundaries is called Contour Dynamics (CD) and has proven to be suitable for calculating vortex interactions in inviscid fluids.[6] Important properties are that the area enclosed by the contours is constant and that their topology is conserved. The conditions under which such a description is valid are met when the fluid equations are of *Lagrangian* form.

A number of (quasi) two-dimensional models for ideal plasmas and fluids can be cast into a Lagrangian form that describes the fluid by the incompressible advection of one or more conserved quantities. These *generalized vorticities* ω_α are pointwise conserved:

$$\frac{\partial \omega_\alpha}{\partial t} + \mathbf{v}_\alpha \cdot \nabla \omega_\alpha = 0, \tag{1}$$

where the subscript α represents the type of generalized vorticity. Each vorticity field ω_α is advected by the velocity field $\mathbf{v}_\alpha$,

$$\mathbf{v}_\alpha = \mathbf{e}_z \times \nabla \Phi_\alpha. \tag{2}$$

To close the set of equations the generalized vorticities are given as functionals of the streaming potentials Φ_α. Inverting these relations yields equations for the potentials in terms of the vorticities.

The equations are in two dimensions. The third direction $\mathbf{e}_z$ is either ignored because the system is approximately of zero thickness in that direction (e.g., atmospheric flows, shallow fluid layers, soap films) or the system is homogeneous in that direction, e.g., for a plasma in a strong magnetic field all quantities may be taken constant to a first approximation in the direction of the field. The simplest example is the Euler equation for two-dimensional incompressible fluid flow which is of form (1) where the fluid vorticity ω and the stream function Φ are related through the Poisson equation $\nabla^2\Phi = \omega$. Inversion yields the long-range logarithmic potential of hydrodynamic vortices.

Another well known example is the Charney–Hasegawa–Mima equation, which describes both quasigeostrophic flows in the atmosphere and drift phenomena in plasmas. The relation between conserved (potential) vorticity and stream function is given by the nonhomogeneous Helmholtz equation $\nabla^2\Phi - \Phi = \omega$. Therefore, the interaction poten-

[a]Present address: Netherlands Organisation for Applied Scientific Research (TNO), P.O. Box 96864, 2509 JG The Hague, The Netherlands. Electronic mail: L.P.J.Kamp@tue.nl

tial of geostrophic vortices is given by the short-range modified Bessel function K_0 (McDonald function).

In the ideal case where physical dissipation is disregarded, which we consider in this paper, the system of equations (1) and (2) contains infinite sets of integrals of the motion, namely, integrals of any function of each generalized vorticity over the domain (Casimir functionals). This implies that contours cannot be broken and/or reconnected so that their topology is conserved. In the case of patches of constant vorticity, these sets reduce to the conservation of the areas of the patches.

The plasma model considered here, describes a quasineutral plasma in a strong background magnetic field.[5,7] The dominant field makes a two-dimensional description possible. Both electrons and ions experience an $\mathbf{E}\times\mathbf{B}$ drift. In addition, the electrons move along the perturbed magnetic field lines and the ions undergo a polarization drift. The associated macroscopic equations, the drift-Alfvén model, can be cast in Lagrangian form and describe the incompressible advection of three generalized vorticities, each by its own velocity field. These generalized vorticities are not directly physical quantities, but are linear combinations of the generalized parallel momentum, the vorticity of the $\mathbf{E}\times\mathbf{B}$ motion, and of the plasma density. The three streaming potentials are linear combinations of the electrostatic potential and the magnetic flux function. The system contains two length scales, the electron inertial skin depth d_e and the ion sound gyroradius ρ_s.

In the drift-Alfvén model the relations between stream functions and vorticities consist of a combination of the Poisson and Helmholtz operators, resulting in an interaction that is a mixture of the long- and short-range potentials mentioned above. Generalizing the method of Contour Dynamics to handle three different types of vorticity rather than just one as in the nonconducting fluid case, the present paper explores the consequences of this mixture of long- and short-range interaction between FAVRs. The two main results to be presented are as follows.

(A) The competition between the two contributions to the interaction potential has an important effect on the dynamics of vortex motion in the plasma. It introduces a length scale where the long-range potential "takes over" from the short-range potential. This length is $O(d_e)$. When the inertial skin depth d_e is smaller than the ion sound gyroradius ρ_s, the two contributions induce velocities with opposite directions. As a consequence structures on a scale $O(d_e)$ will be formed either by merging smaller vortices or by splitting of larger vortices. It gives also rise to quasiperiodic splitting-merging cycles.

(B) In the interaction between patches of unequal type two interaction potentials play a role: first the interaction of one vortex on itself and second the interaction between the two types of vorticity. Depending on the parameters, the flow given by these interaction potentials can give rise to different splitting/merging behavior compared to the interaction of equal-type vortices.

Vortices of unequal type are allowed to overlap. In particular, by overlapping vortices we can create distributions with current density only, corresponding to current wires along the magnetic field in the plasma. Of special interest in confined plasmas—which are usually dominated by magnetic effects and processes—is the merging interaction of two like-signed parallel currents, which has been analyzed in Ref. 8. Such currents attract each other by the Lorentz force. A flow pattern is generated which merges the currents. The plasma shields the currents on distances of the order of the electron inertial skin depth d_e, so that the interaction is exponentially weak when the initial separation of the currents is large.

A short introduction and a discussion of the plasma model is presented in Sec. II and Appendix A. The interaction potential between elements of generalized vorticity is introduced and its relation with the induced velocity field is discussed. In Sec. III we discuss the CD method for the present plasma model. Additional details of the numerical CD code are given in Appendix B. We also introduce contour surgery, an extension of the CD method, in order to perform long-time calculations. A numerical analysis of the dynamics of a single elliptical patch is presented in Sec. IV. The directions of rotation are discussed. The emphasis is on the occurrence of quasiperiodic splitting-merging cycles. The interactions between vortex *pairs* and *dipoles*, i.e., between two patches with strengths of equal and opposite sign, are studied in Sec. V. The dynamics of pairs and dipoles of both equal and mixed type of generalized vorticity is analyzed.

II. THE DRIFT-ALFVÉN MODEL

We consider a low-β plasma, immersed in a strong magnetic field given by

$$\mathbf{B} = B_0[\mathbf{e}_z + \mathbf{e}_z \times \nabla \psi(\mathbf{x},t)]. \tag{3}$$

The flux function ψ describes field line bending. Field line compression is neglected. The electric field is

$$\mathbf{E} = -\nabla \phi + \frac{B_0}{c}\frac{\partial \psi}{\partial t}\mathbf{e}_z. \tag{4}$$

The electron temperature T_e is taken to be constant throughout the fluid. The ion current along the strong field $\mathbf{B}_0$ is neglected. In what follows, we consider two-dimensional motions, all quantities are assumed to be independent of the z coordinate, i.e., $\mathbf{x}=\mathbf{r}=x\mathbf{e}_{x+y+y}\mathbf{e}_y$.

Neglecting third-order nonlinearities, the equations that describe the electron and ion fluids can be cast in form (1) for three generalized vorticities; each vorticity field is advected by its corresponding velocity field (2) (see Appendix A). This system contains two length scales, the electron inertial skin depth d_e and the ion sound gyroradius ρ_s,

$$d_e = \sqrt{\frac{m_e c^2}{4\pi n e^2}}, \quad \rho_s = \sqrt{\frac{T_e}{m_i \Omega_i^2}}. \tag{5}$$

Next we normalize the length scale on the ion sound gyroradius, the time on the ion cyclotron frequency $\Omega_i = eB_0/m_i c$, and introduce the normalized quantities

$$N = \frac{n}{n_0}, \quad \Phi = \frac{e\phi}{T_e}, \quad \Psi = v_A \frac{eB_0}{cT_e}\psi, \tag{6}$$

n_0 being a reference value of the density and $v_A = B_0/\sqrt{4\pi n_0 m_i}$ the Alfvén velocity. In terms of these normalized quantities, the three generalized vorticities $\omega_\alpha(\alpha = +, -, 0)$, are given by

$$2\lambda_e \omega_\pm = \lambda_e N \pm (\Psi - \lambda_e^2 \nabla^2 \Psi) \tag{7}$$

and

$$\omega_0 = \nabla^2 \Phi - N, \tag{8}$$

where $\lambda_e = d_e/\rho_s$. The quantity between parentheses on the right represents the z component of the generalized momentum of an electron. Vortices of plus and minus types carry current and vorticity in equal but opposite ratios, while the zero-type vortices carry vorticity only. The Laplacian of the magnetic flux Ψ is the normalized parallel current density, $J = \nabla^2 \Psi$.

The streaming potentials of the incompressible velocity fields $\mathbf{v}_\alpha = \mathbf{e}_z \times \boldsymbol{\nabla} \Phi_\alpha$ are

$$\Phi_\alpha = \Phi + c_\alpha \Psi, \quad \alpha = +, -, 0, \tag{9}$$

with

$$c_\pm = \pm \frac{1}{\lambda_e}, \quad c_0 = 0. \tag{10}$$

The relations between potentials and vorticities are given by

$$\nabla^2 \Phi = \sum_\alpha \omega_\alpha, \tag{11}$$

$$\left(\nabla^2 - \frac{1}{\lambda_e^2}\right)\Psi = -\sum_\alpha c_\alpha \omega_\alpha, \tag{12}$$

and

$$N = \nabla^2 \Phi - \omega_0. \tag{13}$$

When the fields ω_α are given by a distribution of patches, this still allows for a constant background value of the generalized vorticity fields. This changes the streaming potentials but leaves the dynamical equations (1) in Lagrangian form. In this work we only consider fields that are generated by the patches themselves, i.e., we assume the external fields to be zero. Moreover, in this paper we will analyze the dynamics of patches of $\omega_\pm$ vorticity and take $\omega_0 = 0$, i.e., $N = \nabla^2 \Phi$; this excludes electrostatic drift vortices.

The energy integral of the system is given by

$$W = \frac{1}{2}\int d^2x [|\boldsymbol{\nabla} \Psi|^2 + \lambda_e^2 J^2 + N^2 + |\boldsymbol{\nabla} \Phi|^2]$$

$$= -\frac{1}{2}\int d^2x \sum_\alpha \Phi_\alpha \omega_\alpha + \int d^2x (\omega_-^2 + \omega_+^2). \tag{14}$$

The four terms in the integrand in the first expression for the energy represent the magnetic energy, the parallel kinetic energy of the electrons, the internal electron energy, and the perpendicular kinetic energy of the ions, respectively. The first contribution of the second expression for the energy is a generalization of the Hamiltonian functional for the Euler equation.[5] The second contribution is a Casimir and the generalization of the entrophy.

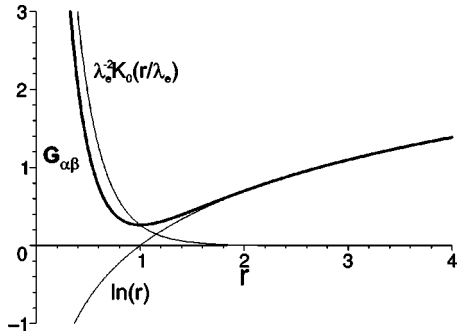

FIG. 1. The mixed Green's function $G_{\alpha\beta}$ for $c_\alpha c_\beta > 1$ and $\lambda_e = 0.3$.

Besides the Casimirs and the energy, the system might also preserve linear momenta and/or angular momentum. This depends on the symmetry of the initial conditions and of the boundary conditions.

A. The interaction potential

Inverting the relations (11) and (12), and using Eq. (9), one obtains the streaming potentials Φ_α as integrals over the vorticity distributions $\omega_\alpha(\mathbf{r})$:

$$\Phi_\alpha(\mathbf{r}) = \sum_\beta \int G_{\alpha\beta}(|\mathbf{r} - \mathbf{r}'|)\omega_\beta(\mathbf{r}') d^2 r'. \tag{15}$$

The Green's function for an unbounded domain is given by

$$G_{\alpha\beta}(r) = \frac{1}{2\pi}\left[\ln r + c_\alpha c_\beta K_0\left(\frac{r}{\lambda_e}\right)\right]. \tag{16}$$

Here, K_0 is the zeroth-order Bessel function of the second kind. The Green's function itself represents the stream function of type α at $\mathbf{r}$ due to a single vorticity element of type β at $\mathbf{r}' = 0$. The interaction potential (16) has a mixed character of both a long-range logarithmic interaction known from incompressible planar hydrodynamics and a short-range modified Bessel interaction as in the Charney–Hasegawa–Mima model. In the limit $r \gg \lambda_e$ the modified Bessel function vanishes exponentially, so that $G_{\alpha\beta} \sim (2\pi)^{-1} \ln r$. For $r \ll \lambda_e$ also the modified Bessel function is mainly logarithmic and combines with $\ln r$, so that $G_{\alpha\beta} \sim (2\pi)^{-1}(1 - c_\alpha c_\beta)\ln r$. Since $c_\alpha c_\beta = \alpha\beta/\lambda_e^2$, the interaction potential has a minimum if $\alpha = \beta$ and λ_e^{-2}. Such a minimum does not exist in the interaction potential between elements of unequal vorticities ($\alpha \neq \beta$). In Fig. 1 the behavior of the Green's function is plotted for $\lambda_e = 0.3$. The minimum in the interaction potential $G_{\alpha\beta}$ gives rise to a change in sign of the azimuthal velocity field.

The velocity field induced by a single vorticity element at $\mathbf{r} = 0$ depends on the distance r to this element and on the value of the parameter λ_e and is given by $v_\theta = \partial G_{\alpha\beta}/\partial r$. A contour plot of $v_\theta(r, \lambda_e) = 0$ is presented in Fig. 2. Crossing the boundary between the unshaded and the shaded area results in a change in sign of the velocity field generated by the point vortex.

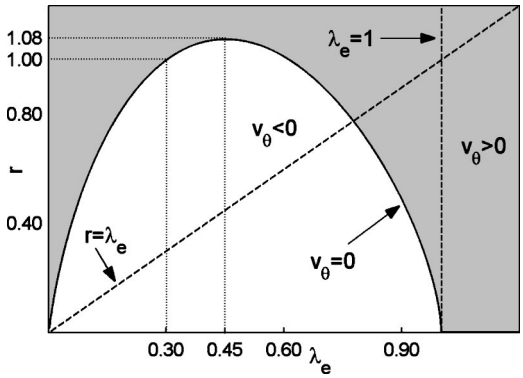

FIG. 2. Contour plot of the azimuthal velocity field $v_\theta(r,\lambda_e)=0$ generated by a point vortex at $\mathbf{r}=0$. The velocity vanishes on the curve $r=r(\lambda_e)$.

In case of a single patch of a single vorticity type, it follows immediately that for $\lambda_e>1$ all elements of a patch rotate in the same (counterclockwise; $v_\theta>0$) direction. For $\lambda_e<1$, elements can rotate either clockwise ($v_\theta<0$) or counterclockwise ($v_\theta>0$), depending on the size of the patch. If the patch size is small enough all elements rotate clockwise, i.e., $v_\theta<0$, which corresponds to the unshaded area in Fig. 2. For larger patches not all elements rotate in the same direction. Actually, in that case, there is a competition between the two rotation directions. This is of particular interest and will be discussed in Sec. IV of this paper.

B. The fields of a circular patch

Consider a single, circular patch of generalized vorticity of either plus or minus type. Inside a radius R the vorticity is equal to $\omega_\beta=\kappa$, outside it vanishes. Upon using polar coordinates (r,θ) with the center of the patch at the origin, one obtains from Eqs. (11) and (12) the localized solution

$$\Phi=\begin{cases}\dfrac{\kappa}{4}(r^2-R^2) & \text{for } r<R\\[2ex] \dfrac{\kappa}{2}R^2\ln\left(\dfrac{r}{R}\right) & \text{for } r>R\end{cases} \tag{17}$$

and

$$\Psi=\begin{cases}c_\beta\kappa\lambda_e^2\left[1-\frac{R}{\lambda_e}K_1\left(\dfrac{R}{\lambda_e}\right)I_0\left(\dfrac{r}{\lambda_e}\right)\right] & \text{for } r<R\\[2ex] c_\beta\kappa\lambda_e R\, I_1\left(\dfrac{R}{\lambda_e}\right)K_0\left(\dfrac{r}{\lambda_e}\right) & \text{for } r>R,\end{cases} \tag{18}$$

where $I_{0,1}$ and $K_{0,1}$ are modified Bessel functions and the Wronskian $I_0(x)K_1(x)+I_1(x)K_0(x)=1/x$ is used. The streaming potentials $\Phi_\alpha(r,\theta)$ are obtained from Eq. (9); the purely azimuthal velocity $\mathbf{v}_\alpha$ is given by $\mathbf{e}_\theta\partial_r\Phi_\alpha$. From Eqs. (11)–(13) we find $J,\nabla^2\Phi$, and N. An illustration of the fields of an ω_+ patch for the case $\lambda_e=0.3$ is given in Fig. 3. We stress the following aspects.

(i) Although only ω_+ is unequal to zero, velocity fields of all three types are present.
(ii) Quite trivially, the three velocity fields, the current, the fluid vorticity, and Φ and Ψ all change sign when the strength κ of the patch is changed to $-\kappa$.

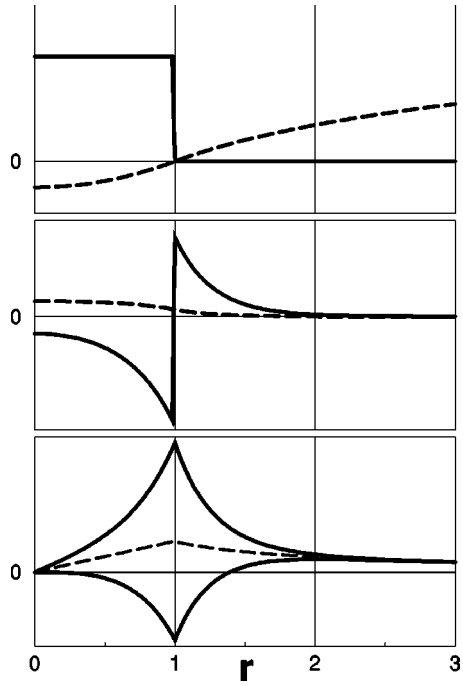

FIG. 3. Fields of a circular ω_+ patch with radius $R=1$ for $\lambda_e=0.3$. (Upper panel) the vorticity of the $\mathbf{E}\times\mathbf{B}$ flow (solid line) and the electrostatic potential Φ (dashed line); (middle panel) the current density J (solid line) and the flux function Ψ (dashed line); (lower panel) the three azimuthal velocity fields $\mathbf{v}_\pm$ (solid lines) and $\mathbf{v}_0$ (dashed line). The latter is the $\mathbf{E}\times\mathbf{B}$ velocity field.

(iii) Of the given velocity fields only $\mathbf{v}_+$ changes sign as a result of the mixed nature of the Green's function.
(iv) Magnetic Lorentz forces are screened on a distance of the order λ_e.
(v) For an ω_- patch instead of an ω_+ patch, the potential Φ and the fluid vorticity do not change, but the flux ψ and the current J do change sign.

By overlapping patches of unequal type, two physically relevant systems can be modeled: pure vorticity and pure current distributions.

A pure vorticity distribution is obtained when $\Sigma c_\alpha\omega_\alpha=0$ everywhere. In the absence of external fields we have $J=0$ and $\Psi=0$. The streaming potentials are all identical, $\Phi_\alpha=\Phi$, so all patches are advected by exactly the same velocity field. This means that when $t=0$ the patches are overlapping such that there is vorticity only; the flow will never change that. There will be no generation of current density and transverse magnetic field and the evolution of the vorticity is governed by the Euler equation.

More interesting dynamics is found in the case of a pure current distribution. To that end a distribution is assumed for which initially $\nabla^2\Phi=0$. The condition for this is $\Sigma\omega_\alpha=0$ everywhere. A simple current distribution is constructed by taking $\omega_+=-\omega_-=\kappa$ inside a circular contour of radius R and zero outside. The field ω_0 is zero everywhere, so that $N=\nabla^2\Phi$. At $t=0$ both Φ and $\nabla^2\Phi$ are exactly zero, while Ψ and J are given by

$$\frac{\Psi}{2\kappa} = \begin{cases} \lambda_e - R\,K_1\left(\frac{R}{\lambda_e}\right) I_0\left(\frac{r}{\lambda_e}\right), & J = \frac{\Psi}{\lambda_e^2} - 2\frac{\kappa}{\lambda_e} \quad \text{for } r < R \\ R\,I_1\left(\frac{R}{\lambda_e}\right) K_0\left(\frac{r}{\lambda_e}\right), & J = \frac{\Psi}{\lambda_e^2} \quad \text{for } r > R. \end{cases} \tag{19}$$

These expressions are of the same form as those for the single plus-type patch in Fig. 3 because the current and magnetic flux add up constructively, while vorticity and electric potential vanish. The dynamical interaction between two initially circular shaped current distributions has been analyzed in Ref. 8.

III. CONTOUR DYNAMICS

In this section an outline of the method of CD is given, extending the CD method for inviscid hydrodynamics[3,9] to the case with three, instead of one, conserved vorticities.

Equation (1) contains exact solutions for piecewise uniform distributions of generalized vorticity. Such piecewise uniform vorticity distributions remain piecewise uniform in time. The topology and area of these vorticity distributions, which we call vorticity patches, are conserved. This implies that there is deformation of the boundaries of the patches only. Hence, the evolution can completely be described in terms of the motion of the boundaries. This forms the essence of the method of Contour Dynamics.

In the numerical calculations the vorticity distribution for each type is taken to be piecewise constant. Each region $\Gamma_{\alpha,m}$ of constant vorticity $\hat{\omega}_{\alpha,m}$ is bounded by a contour $\gamma_{\alpha,m}$. We choose $\hat{\omega}_{\alpha,0}=0$ for $\mathbf{r} \in \Gamma_{\alpha,0}$, the exterior of the vorticity distribution. The jump in vorticity crossing contour $\gamma_{\alpha,m}$ inward is denoted by $\omega_{\alpha,m}$. Contours are counted by $m = 1, \ldots, M_\alpha, M_\alpha$ being the total number of contours of type α. Contours of equal type do not cross each other, but can be nested.

The velocity field with which the distribution $\omega_\alpha(\mathbf{r})$ is advected is given by

$$\mathbf{v}_\alpha(\mathbf{r}) = \mathbf{e}_z \times \boldsymbol{\nabla}_\mathbf{r} \left[\sum_\beta \sum_{m=1}^{M_\beta} \hat{\omega}_{\beta,m} \int_{\Gamma_{\beta,m}} G_{\alpha\beta}(|\mathbf{r} - \mathbf{r}'|) d^2 r' \right]. \tag{20}$$

Inside the integral use $\boldsymbol{\nabla}_\mathbf{r} G = -\boldsymbol{\nabla}_{\mathbf{r}'} G$ and apply Stokes' theorem for a scalar field. We then arrive at

$$\mathbf{v}_\alpha(\mathbf{r}) = -\sum_\beta \sum_{m=1}^{M_\beta} \omega_{\beta,m} \oint_{\gamma_{\beta,m}} G_{\alpha,\beta}(|\mathbf{r} - \mathbf{r}'|) d\mathbf{l}'. \tag{21}$$

This equation gives the three velocity fields at each point of the plane, in particular, at the points of the contours themselves. The motion of the contours, and thus of the vorticity distribution, is completely given by Eq. (21). Because the velocity fields $\mathbf{v}_\alpha$ are divergence-free, the area enclosed by each contour is constant.

To evaluate the fields at a certain point when a complete set of contours is given, we evaluate the sum of two-dimensional integrals (15) numerically to find the streaming potentials. By determining whether the point lies in or outside a contour, one knows the generalized vorticities at that point. Subsequently, from Eqs. (9) and (11)–(13) we find the physical fields.

Although the contour dynamics code can handle sets of nested contours so that patches with distributed vorticity can be simulated, in this paper we will restrict ourselves to patches with uniform vorticity each of which is defined initially by a single contour. The contours of the patches are discretized by using a finite but dynamically adjustable number of nodes. Between the nodes, the contours are approximated by linear line segments. It is shown in Ref. 9 that the velocity field induced by the discretized system is still divergence-free. This implies that it retains the Hamiltonian character of the original system, in particular, the generalized linking conditions. To advance the position of the contours in time a symplectic integration scheme is applied. This time integration is especially designed to conserve the Hamiltonian character of the dynamics and thus to preserve the constants of the motion of the system, i.e., the areas of the patches. This time stepping algorithm is based on the symplectic midpoint rule and is implemented with a predictor-corrector scheme. If a sufficient large number of predictor-corrector cycles would be applied, the areas of the patches will be conserved up to machine accuracy. In practice the number is limited such that areas are conserved up to 10^{-4}. For more details about the used CD method see Ref. 9.

In most cases contours become increasingly complex in time. In order to keep track of the shape of a curve and to preserve its identity, the number of nodes on a contour varies during a simulation. For example, nodes will be added to a contour when decurvature is above a certain limit, or when contours of equal type approach each other closely. The computational time increases with the square of the number of nodes. More details are given in Appendix B.

The symplectic integration scheme is designed for long-time calculations. However, the contours will often become so deformed and folded that the contour can only be followed during a limited time. In order to be able to compute the dynamics on a longer time scale, contour surgery has been invoked.[6] To that end a surgery module[10] has been implemented with the extended CD code.

When two contours of equal type of vorticity or two parts of the same contour approach each other closely and their mutual distance falls below a critical value, a topological reconnection is made. Locally this results in surgery of the two original curves such that two new curves emerge. Globally the number of contours may change. When two different contours approach each other, surgery decreases the number of contours by one (merging). When two parts of the same contour approach each other, surgery will increase the number of contours by one (splitting).

Due to surgery, quite often very small contours emerge that contain a small fraction of the total area. The contribution of such contours to the velocity field is small, while they may contain a large number of nodes. Therefore, when the area enclosed by a contour is below a critical fraction of the total initial area, the contour is removed. The surgery process might lead to an increase as well as to a decrease of the enclosed area. Consequently, the total circulation of the gen-

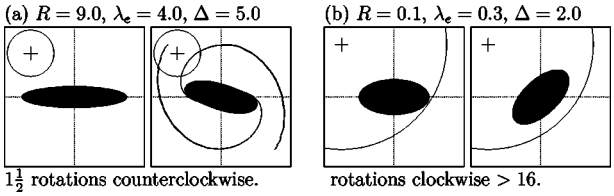

FIG. 4. First and last time steps of counterclockwise (a) and clockwise (b) rotating patches. The relative magnitude of λ_e is indicated by the radius of the unshaded circles, R and Δ denote the semimajor axis and aspect ratio of the initial ellipse, respectively.

eralized flow field as well as all Casimirs are not constant in time anymore and will vary slightly during a computational run.

To measure the accuracy of our code, the area enclosed by each contour is calculated at every time step. After the simulation the absolute value of the sum of the areas S_n gained or lost in the process,

$$\frac{\delta S(N)}{S_0} = \frac{1}{S_0}\sum_{n=1}^{N} |S_n - S_{n-1}|, \tag{22}$$

with $S_1 = S_0$, is evaluated as a function of the number of time steps N. The general trend without surgery is, as may be expected, a gradual increase of the ratio $\delta S(N)/S_0$. The average slope of $\delta S(N)/S_0$ depends on the redistribution of the nodes. For a stable patch such as the one described in Fig. 4(c), $\delta S(N)/S_0$ is of the order of 10^{-5} after 1000 time steps. In situations where a more rich dynamical behavior occurs, the relative error is typically of the order 10^{-3} after 500 time steps.

When surgery sets in, jumps appear in the gradually increasing graph of $\delta S(N)/S_0$. The maximum relative error in the area due to surgery appeared to be less than 1% per step in our simulations. The main contribution to losses due to surgery comes from splitting and merging processes (see, for example, Fig. 13). Only a small fraction is an effect of vanishing filaments. For example in Fig. 9, the jump due to merging is 0.8%, while $\approx$1.3% of the losses appear during the two splitting processes. The total relative error in this simulation is 2.4%.

Losses due to surgery as well as losses due to redistribution of nodes can be reduced by adjusting the parameters such that smaller scales are taken into account. However, such refinements do not change the dynamical behavior of the simulations presented in this paper.

Whereas the CD method is intimately related to the Lagrangian nature of Eqs. (1), other numerical techniques to solve the partial differential equations (11)–(13) may be considered too. In fact a number of the CD simulations to be presented hereafter have been confronted with an alternative numerical integration scheme that is based on the so-called Finite Element (FE) method. In this method the partial differential equations (11)–(13) are discretized on a mesh that consists of triangles. It should be noted that such an integration scheme is not inherently symplectic. Because the equations themselves are Lagrangian, their discretization on a mesh can introduce numerical instabilities in the solution. Therefore, some form of stabilization of the integration scheme is necessary. These stabilization techniques can all be grouped under the name artificial diffusion (artificial viscosity or numerical diffusion/viscosity are also commonly used terms). In a way this artificial diffusion is reminiscent to but not the same as the contour surgery described above. Small-scale structures that are removed during the process of contour surgery are diffused away in the FE method because of the numerical diffusion.

Our FE computations are done with the commercially available software package FEMLAB.[11] With FEMLAB the evolution of patches of constant vorticities is evaluated on a finite domain using the Dirichlett condition on the boundary. The computational domain is chosen such that its boundary is far away from the vorticity patch itself in order to mimic the infinite domain that is inherent to the CD simulations. In a typical run we cover the computational domain with 6×10^4 mesh elements using a much higher mesh resolution near the vorticity patch than elsewhere.

The contributions to the energy, Eq. (14), can be calculated from the values of the fields at each point of a regular grid. Because of the use of a finite area and a finite grid spacing, the calculated energy is not exactly conserved. Both large (the fields outside the grid region) and small scales (features which are smaller than the grid spacing) may lead to an increase or reduction of the calculated energy. This procedure does not influence the dynamical evolution of the system.

IV. SINGLE PATCHES

In this section we present numerical simulations of the motion of single vorticity patches of the plus type. The system contains as dynamical parameters the electron inertial skin depth λ_e and the vorticity ω_+. We recall that all length scales are scaled on ρ_s, so actually d_e and ρ_s are the two spatial parameters of our system. In addition, there are geometrical parameters that specify the initial sizes and shapes of the patches. The structure of the equations shows that a scaling to larger vorticity implies a scaling to shorter times. Moreover, we note that the results of this section also apply to patches of the minus type.

A. Rotating patches

In the discussion on the interaction potential (16) we concluded that there can be clockwise as well as counterclockwise rotating structures. Vorticity elements with a mutual distance below $r(\lambda_e)$ (see Fig. 2) will induce clockwise rotations, while vorticity elements on a larger distance induce counterclockwise rotations. In this section both rotation directions are demonstrated by simulating the behavior of a single patch.

Since circular patches are linearly stable,[12] we start the simulation with an elliptic patch of uniform vorticity. The semimajor axis and aspect ratio are denoted by R and $\Delta \geqslant 1$, respectively. It was shown by *Kirchhoff* that in the Euler case, i.e., in the limit $r \gg \lambda_e$ of the interaction potential (16), elliptic patches that steadily rotate counterclockwise with angular frequency[13–15]

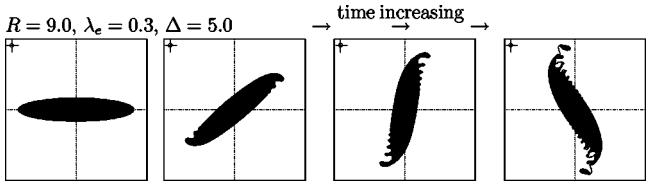

FIG. 5. A patch that induces filaments on the edge due to competition between small-scale clockwise rotation and large-scale counterclockwise rotation. The patch as a whole rotates about 3/8 times counterclockwise during the simulation.

$$\Omega = \omega_\alpha \frac{\Delta}{(1+\Delta)^2} \tag{23}$$

are exact solutions. These solutions are stable[13,15] if and only if $\Delta < 3$. In the limit $r \ll \lambda_e$ the interaction potential is again logarithmic, however with multiplicative factor $(-1+\lambda_e^{-2})$. As a result, for $\lambda_e < 1$ the patch will rotate in the direction opposite to the one in the Euler limit and with frequency $(1-\lambda_e^{-2})\Omega$.

Figure 4 shows the time evolution of two cases. Figure 4(a) shows the evolution of a patch with $R=9.0$, $\lambda_e=4.0$, and $\Delta=5.0$. For these values the logarithmic interaction is dominant and the global as well as local rotation is counterclockwise. In this and all other figures in this paper, the relative magnitude of λ_e is indicated by the radius of an unshaded circle. The global rotation frequency is in agreement with Eq. (23). Just as in hydrodynamic cases, filaments appear, in this case after 3/4th of the global revolution time. Figure 4(b) represents the time evolution of an initially elliptical patch with $R=0.1$, $\lambda_e=0.3$, and $\Delta=2.0$. For these values of the parameters the Bessel function in Eq. (16) may be approximated by a logarithm and the interactions between all parts of the patch correspond to the area below the curve $v_\theta(r)=0$ of Fig. 2. As a consequence, all parts of the patch rotate in the clockwise direction. The angular frequency of the global structure is well approximated by $(1-\lambda_e^{-2})\Omega$ as has been verified from numerical results from CD and FE computations. This patch is stable for at least 16 revolutions.

A simulation where the competition between the two possible rotation directions of a patch is clearly visible is presented in Fig. 5. Since the size R of the patch is large, its global rotation is induced by the logarithmic interaction and is counterclockwise with frequency Ω. In contrast to Fig. 4(a), however, $\lambda_e < 1$ in this case, so that on a small scale the Bessel interaction becomes important and a trade off occurs between clockwise and counterclockwise rotations, as has been discussed in Figs. 1 and 2. This is visible in the instability that develops along the contour and that leads to the generation of small-scale blobs at the boundary of the patch. These small-scale structures rotate in the clockwise sense. They tend to move away from the patch to form small isolated satellite patches. The size of these more or less isolated blobs is of the order of λ_e.

For $\lambda_e=0.3$, the distance at which the rotation induced by a vorticity element vanishes is $r(\lambda_e) \approx 1.0$. Thus, for patches with size $R=O(1)$, the competition between clockwise and counterclockwise rotations will extend over the whole patch. This is illustrated in Fig. 6 where the evolution of an elliptical patch with $R=1.5$, $\lambda_e=0.3$ for $\Delta=4.0$ is presented. The evolution shows an almost periodic constriction and broadening near the origin and a very slow, global, and clockwise rotation.

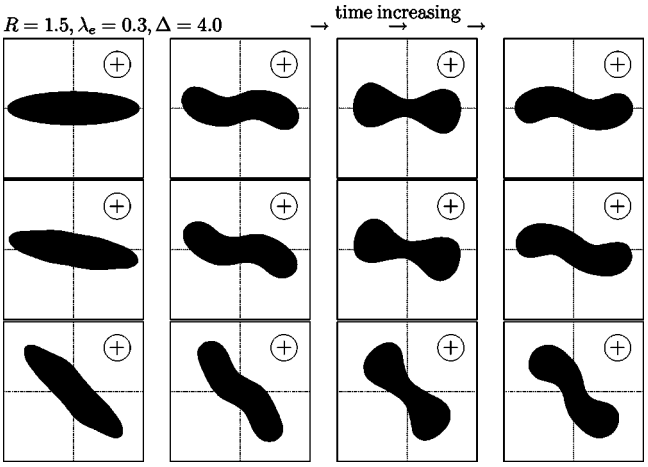

FIG. 6. A periodic motion with a slow global rotation in the clockwise direction. The first, second, and sixth contraction cycle, respectively, are shown.

Although the patch does not actually reach an equilibrium state, globally it is close to a stationary oscillating state. The periodic constriction is not sufficiently strong such that separate patches will be generated. This periodic behavior and slow rotation pertains for smaller values of the ellipticity Δ and for smaller values of R. For sufficiently large values of Δ, the patch will split into two parts (see following section). For smaller values of R the clockwise rotation becomes faster, while for larger values of R the system will tend to show a behavior analogous to that shown in Fig. 5.

B. Splitting and merging

For parameter values as in Fig. 6, the periodic constriction near the origin is not strong enough to cause a split up of the original patch. However, due to the steepness of $G_{\alpha\beta}$ for small r, for slightly different parameter values the shear in the velocity field might be strong enough to lead to splitting of the patch.

The evolution of a patch with $R=1.0$, $\lambda_e=0.3$ for $\Delta=5.0$ is given in Fig. 7. The figure demonstrates that the original patch tends to split into two patches each of size λ_e. The global structure and the separate patches all rotate clockwise. The rotation of the global structure is much slower than the splitting process.

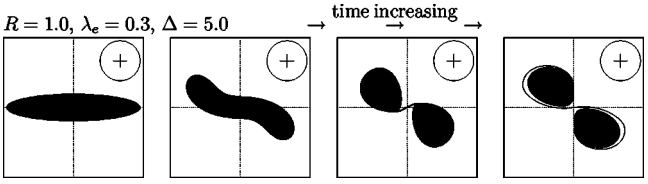

FIG. 7. A patch splitting up in parts with scale λ_e.

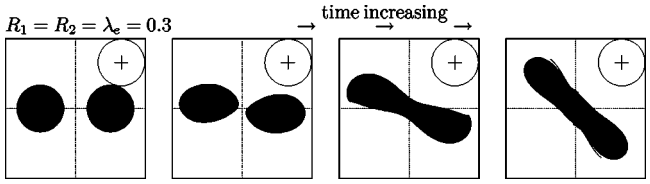

FIG. 8. Merging of two equal patches with scale and distance of order λ_e.

A comparison of Figs. 6 and 7 suggests that, in the latter case, the phase of splitting up might be followed by a merging process, and hence a kind of cyclic process might be possible. However, the results presented up to now in this paper are obtained with the CD code, where contour surgery has not been used. Since topology is conserved as long as contour surgery is absent and therefore contours cannot break up, eventually the calculation breaks down when increasingly long and thin filaments and streamers are formed as in Fig. 7.

Before we invoke contour surgery in order to perform long-time simulations and to investigate the possible occurrence of quasiperiodic splitting-merging cycles, we consider the motion of two circular patches of equal vorticity and both with radius $R=\lambda_e$. The distance L between the centers of the patches is set to $3\lambda_e$. This system resembles the final state in Fig. 7. Although each patch in itself is stable, their interaction deforms their shape and the system as a whole is unstable.

It is known from hydrodynamics, where the Green's function is $G=(2\pi)^{-1}\ln r$, that for a corotating pair not too far apart, the vortices deform and wrap around each other, forming a single, larger vortex.[3,16] Around this structure thin strands of vorticity will develop. These filaments are a common phenomenon in two-dimensional vortex dynamics. The whole process is known as vortex *merging*.

In the case presented in Fig. 8, the mutual distances are small and the Green's function may be approximated by a logarithm, $G\sim(2\pi)^{-1}(1-\lambda^{-2})\ln r$. The figure demonstrates that indeed a merging process takes place at length scale λ_e. The sense of rotation of the pair is opposite to that of two hydrodynamical vortices. The two patches tend to rotate around a common center, but merge far before a single revolution is completed.

In order to describe processes such as the one shown in Fig. 7, on a longer time scale, we will employ contour surgery. The results for a single patch are shown in the following figures.

A quasiperiodic splitting-merging process, analogous to the one shown in Fig. 7, is presented in Fig. 9 for an initially elliptic patch with $R=1.5$, $\lambda_e=0.3$, and $\Delta=5.0$. First the patch splits into two parts that remain connected by a thin strand. This strand becomes thinner and longer until it is cut and reconnected on several places by contour surgery. When the surface element enclosed by a remnant of a strand is sufficiently small, it is discarded. During the next stage, the two patches approach again, wrap around each other, and merge. The contours are now winded up "inside" the patch. When they approach each other sufficiently close, contour surgery sets in. After this merging process the patch splits up again. It may be concluded that a quasicyclic splitting-merging process as suggested by Figs. 7 and 8 is indeed possible. The total area lost or gained by the patch during this process is $\delta S(N)/S_0=2.35\%$. Note that the dimensions of the initial patch in Fig. 9 are such that, globally, no rotation at all occurs. For smaller values of the major radius R than in Fig. 7, a clockwise rotation results and splitting no longer occurs. This is illustrated in Fig. 10.

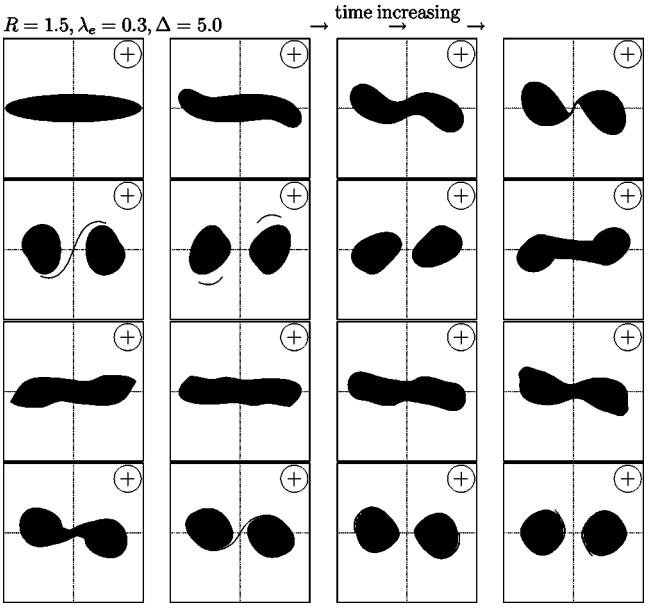

FIG. 9. Splitting-merging process of an initially elliptic patch.

Figures 11 and 12 show the evolution of an initially elliptic patches with aspect ratio $\Delta=4.5$ and $\Delta=4.7$, respectively. The size R of the patches and the values of λ_e are identical to those in Fig. 7. Hence Figs. 7, 11, and 12 are cases with the same values of R and λ_e, but different values of Δ. Upon comparing these figures it is seen that the contraction becomes weaker and the initial patch does not split up anymore for smaller values of the aspect ratio Δ. For larger values the patch splits into three patches, all of the same size.

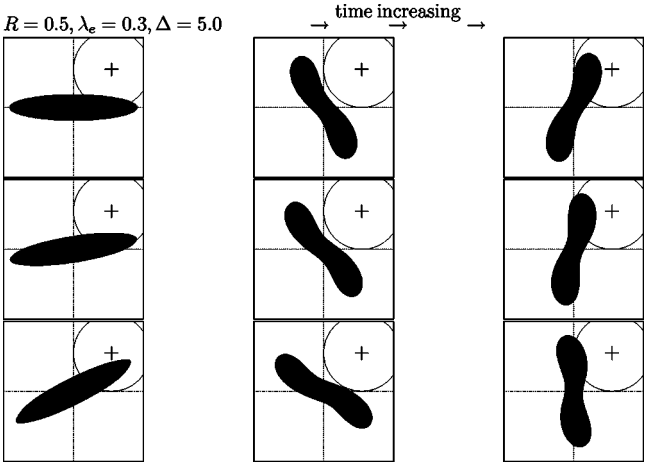

FIG. 10. The first, second, and fourth cycle of a periodically contracting patch. The patch rotates in the clockwise direction.

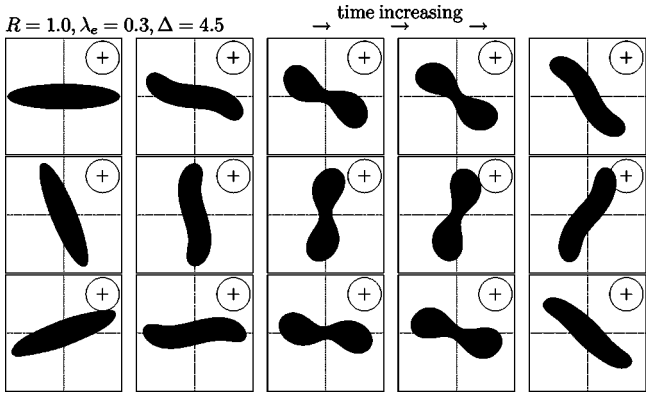

FIG. 11. First, second, and sixth cycle of a quasiperiodic motion with a slow global rotation (clockwise).

If the calculation of the case presented in Fig. 12 is continued in time, numerical errors trigger the growth of asymmetric motions in the system. Finally the patch splits up in one larger and a smaller patch. The smaller one has a size of $O(\lambda_e)$. The larger patch has a smaller size R and a smaller aspect ratio Δ than the original patch. Each of the two patches, the larger as well as the smaller one, seem to undergo a stable rotation. Furthermore, the system of these two patches as a whole undergoes a steady clockwise rotation. In fact this is one of those simulations that have been confronted with a simulation using the previously described FE method and the results of that FE run for early times are shown in the insets in Fig. 14(a). Although the final state resulting from the FE computation is qualitatively the same as the one computed with the CD method, this final state is reached much earlier in time than with the FE run. We attribute this to the fact that in the FE method the vorticity within the boundary of the FAVR is not per definition constant as it is in the CD method but rather fluctuates in space and time due to numerical errors. In general this may lead to

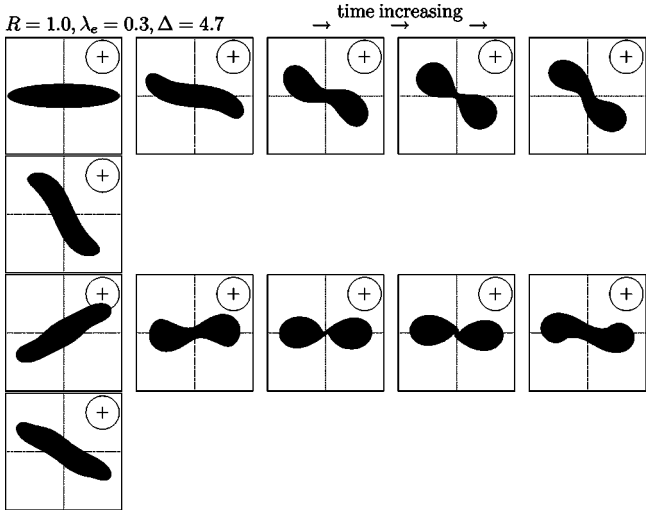

FIG. 12. A periodic motion with a slow global rotation. The first six figures represent the first, and the last six the third contraction cycle. This third contraction cycle shows a splitting-merging phenomena that involves contour surgery resulting in a sudden increase in the normalized error $\delta S(N)/S_0$ (see Fig. 13).

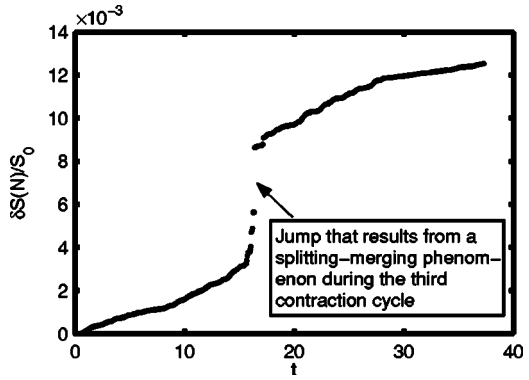

FIG. 13. The normalized error $\delta S(N)/S_0$ in the area of the patch is shown here. The jump in the error takes place during the third contraction cycle that is shown in Fig. 12 and is also indicated by an arrow in Fig. 14(a). The vorticity inside the patch is set to one.

asymmetries in the vorticity distribution resulting in the mentioned observed differences between both methods.

Figure 13 shows the normalized sum $\delta S(N)/S_0$ as calculated with Contour Dynamics for the case in Fig. 12. Note that $\delta S(N)/S_0$ is analogous to the normalized enstrophy, in the sense that all changes in this Casimir are taken with the same sign. The jump in the error can be attributed to the only splitting-merging phenomenon that occurred during the simulation time. This splitting-merging event takes place during the third contraction cycle that is shown in Fig. 12 and is also indicated in Fig. 14(a) by means of an arrow. The remaining parts of the error curve describe the gradual deterioration of area conservation due to the formation of singularities at the boundary of the patch

One may expect that the quasiperiodic dynamics of the elliptic patches depicted in Figs. 11 and 12 is reflected in the time behavior of the various energy terms that contribute to the total energy of the system [see Eq. (14)]. That this is indeed the case becomes apparent from Fig. 14 where we show the time behavior of the kinetic energy contained in the $\mathbf{E}\times\mathbf{B}$ drift (a), i.e., $(1/2)\int d^2x|\nabla\Phi|^2=-(1/2)\int d^2x\ \Phi\omega_+$, the magnetic energy (b), i.e., $(1/2)\int d^2x|\nabla\Psi|^2=(1/2\lambda_e)\int d^2x(\omega_+-\Psi)\Psi$, and the parallel kinetic energy of the electrons (c), i.e., $(1/2)\int d^2x\lambda_e^2J^2=(1/2)\int d^2x(\Psi-\omega_+)^2$. These energy contributions have been computed using the FE method to evaluate the evolution of an initially elliptic ω_+ vorticity patch with $R=1$, $\lambda_e=0.3$, and $\Delta=4.7$. We do not show the fourth term that contributes to the total energy and which is given by $(1/2)\int d^2x\ N^2=(1/2)\int d^2x\ \omega_+^2$ because this is a Casimir functional and therefore constant in time. The numerical evaluation of this Casimir functional using the FE method results in a gradual increase of the integral in due course as a result of numerical errors. In order to circumvent these numerical errors in the evaluation of the parallel kinetic energy of the electrons, we have replaced the contribution $\int d^2x\ \omega_+^2$ to this energy term by its value at $t=0$. This means that we have actually calculated the generalized Hamiltonian functional instead of the total energy in Eq. (14). In the FE code, this contribution is much better conserved than the total energy.

Obviously the three energy contributions show an oscil-

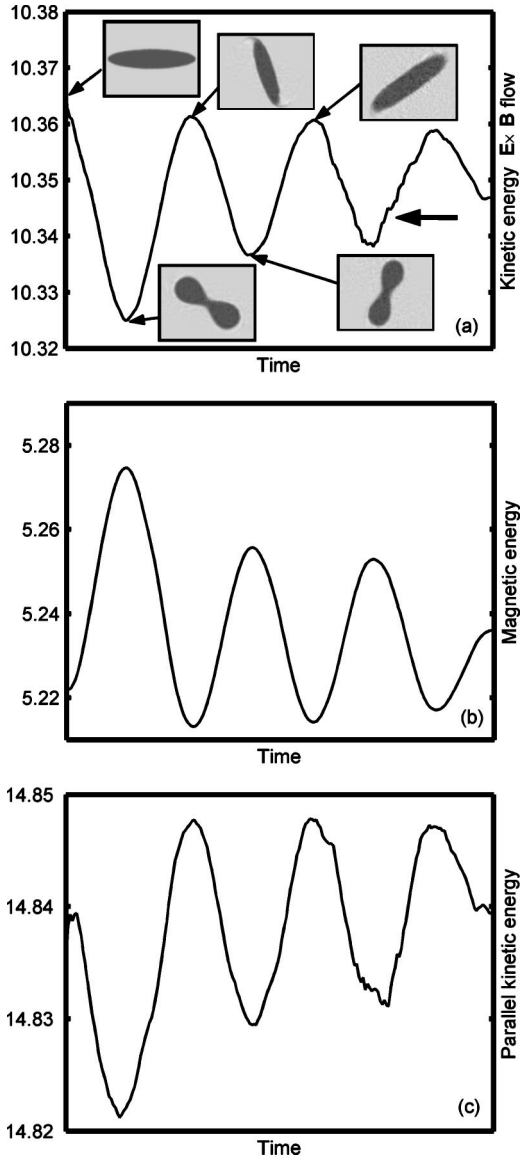

FIG. 14. Periodic behavior of the perpendicular kinetic energy of the ions (a), of the magnetic energy (b), and of the parallel kinetic energy of the electrons (c) for the vorticity patch of Fig. 12. The insets in (a) show snapshots (computed with the FE method) of this vorticity patch at those instants in time when the energy contributions become extreme. The boldface arrow in (a) indicates the third contraction cycle where a splitting-merging phenomena event takes place.

latory behavior that has the same pace as the quasiperiodic contraction of the vorticity patch as shown in Fig. 12. Magnetic energy becomes maximum/minimum whenever the contraction, and thus the separation between current channels, becomes maximum/minimum. For the kinetic energies it is the other way around. The sum of the three time-dependent energy terms that are presented in Fig. 14 has been shown to be constant in time within 0.01%.

V. THE INTERACTION OF TWO PATCHES

In the following it will be useful to distinguish between *internal* and *external* interactions of patches. The internal interaction is the interaction of one part of a (deformed) patch with another part of the same patch. Within the context

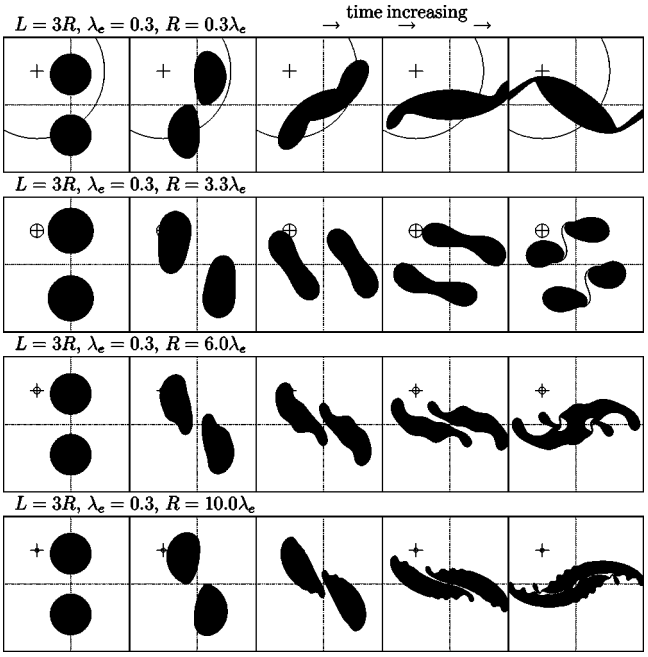

FIG. 15. Interaction of two equal-strength circular ω_+ patches for several values of R/λ_e. The radius of the thin circle indicates the length $\lambda_e=0.3$.

of Contour Dynamics this is the interaction of a contour with itself. The external interaction is the interaction of one vortex patch with another. This distinction will play an important role in the analysis of vortex pairs and dipoles of mixed vorticity type.[17] The interaction potential corresponding to an internal interaction or to an external one of patches with the same vorticity, $G_{\pm\pm}\sim \ln r + c_\pm^2 K_0(r/d_e)$, always has a minimum, while the interaction potential of the external interaction between patches of different vorticities, $G_{\pm\mp}\sim \ln r + c_+c_- K_0(r/d_e)$, has no minimum, so that the velocity induced between vortex elements does not change in sign with their mutual distance.

A. Patches of equal vorticity

First we consider the interaction between two circular current-vortex patches of the plus type. Both have radius R and their centers are a distance L apart. Their strengths are equal, so both have $\omega_+=1$ inside and $\omega_+=0$ outside the patch. The evolution for $\lambda_e=0.3$ and $L=3R$ for several values of R is presented in Fig. 15. The top row shows that small patches with radii below λ_e rotate in the clockwise direction and do indeed merge, as was the case for patches with radii $R=\lambda_e$ shown in Fig. 8.

For larger patches, the mixed nature of the interaction changes the motion. For $R=3.3\lambda_e$ the global rotation of the system is counterclockwise. When the radius becomes larger than a few times λ_e the patches deform each other. Then each of them splits up into smaller structures. In the example for $R=3.3\lambda_e$ given in Fig. 15, each patch splits into two parts that remain connected by thin strands, conserving the initial topology of the two circular vortices. This splitting process is a direct result of the scale length introduced by the minimum in the internal interaction potential. Larger patches show again a merging behavior because both internal and external

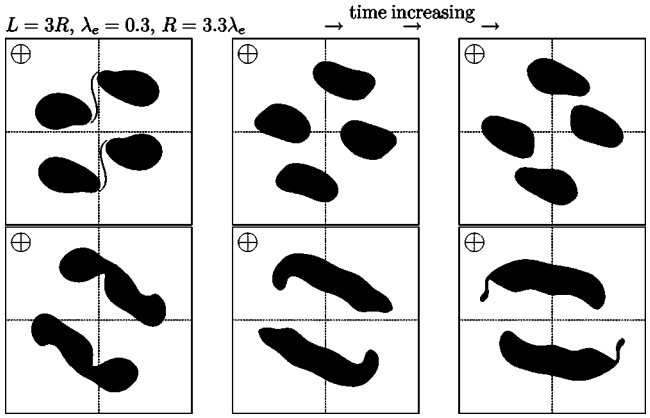

FIG. 16. Long-time interaction of two equal-strength circular ω_+ patches for $L=3R$, $\lambda_e=0.3$, $R=3.3\lambda_e$.

scale lengths are much larger than λ_e. At such distances the current and magnetic field vanish exponentially so that the system behaves globally as an Euler patch. At scales of a few λ_e however, the internal interaction forms structures at the edge of the patches which "flake" off from the large patches, just as in the case of single patches demonstrated in Fig. 5.

The case with $R=3.3\lambda_e$ has been studied for a longer time by employing contour surgery. The result is shown in Fig. 16. After the splitting, each patch rotates in the clockwise direction around its own center of vorticity, while the global rotation is counterclockwise. Subsequently the parts change partners and merge again. At the end of this phase, small blobs split off the main patches. Eventually, like before, the system becomes asymmetric due to numerical errors. This is most pronounced in the FE run that shows the emergence of three quasicircular patches of different sizes but all of the order of the inertial skin depth. Computation with the FE method of the energy contributions (kinetic in the $\mathbf{E}\times\mathbf{B}$ flow, magnetic and parallel kinetic of the electrons) demonstrate that in this case too the three time-dependent energy terms show an oscillatory behavior that keeps pace with the quasiperiodic splitting and merging that is depicted in Figs. 15 (second row) and 16. Magnetic and parallel kinetic energy become maximum after a splitting when the separation between the current channels becomes maximum whereas the perpendicular kinetic energy then becomes minimum. After a merger it is the other way around.

B. Patches of unequal type

Next we consider patches with different types of vorticities but of equal strength. The results are presented in Figs. 17 and 18. For small patches (see Fig. 17), the internal interaction now counteracts the deformation due to the other vortex, so that merging does not take place. Physically, this is an effect of the repulsive force between two oppositely signed currents. This is only clearly seen for small patches because the magnetic interaction is screened at distances larger than λ_e.

For large patches it can be seen that the global motion is determined by the logarithmic term in the interaction, and the evolution strongly resembles that of two patches of equal

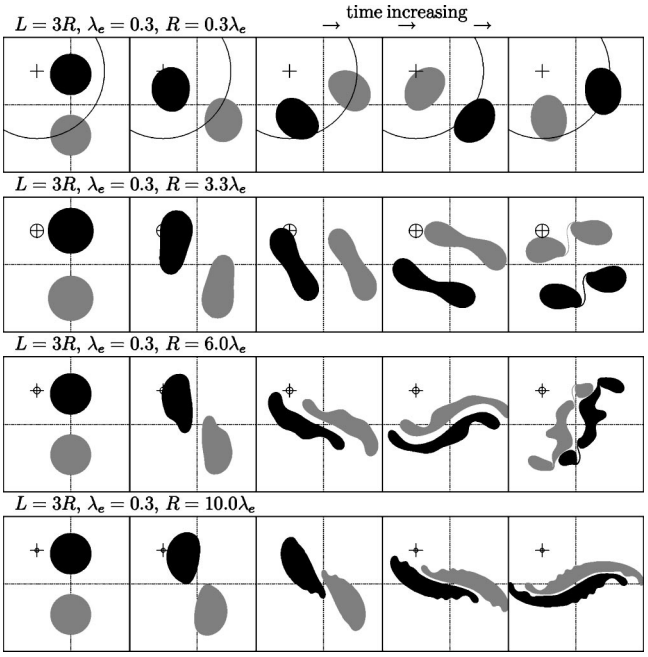

FIG. 17. Interaction of an ω_+ (black) and an ω_- (gray) patch of equal strength.

type. Although there is no topological constraint for patches of unequal type to overlap, in this case the repulsive force between the currents at small distances inhibits such motion.

The splitting off of small structures is seen to be a purely internal process of deformed patches and resembles the evolution of single strongly elliptical patches, which also generate λ_e-scale structures. The interaction with the other vortex merely provides the deformation of the circular patch.

The case $R=3.3\lambda_e$ has been analyzed for longer times using contour surgery. Figure 18 shows the time cycles following the first splitting event. The global rotation of the system is counterclockwise, while each individual patch rotates clockwise around its own center of vorticity. Patches of opposite vorticity do not merge, but after another global half-cycle patches of equal vorticity merge again. At the end of this process small fragments of vorticity are shed from the main patches. A FE run for the same parameters once again shows that eventually the vorticity distribution becomes asymmetric.

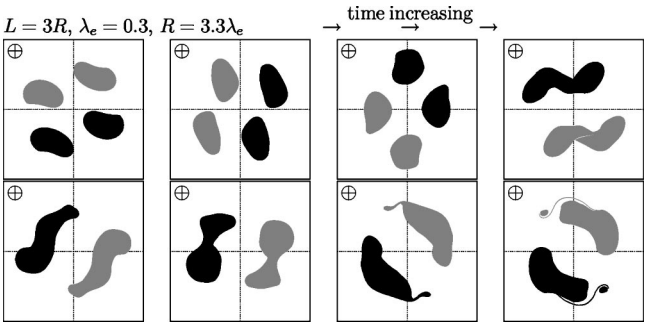

FIG. 18. Long-time interaction of an ω_+ (black) and an ω_- (gray) patch of equal strength for $L=3R$, $\lambda_e=0.3$, $R=3.3\lambda_e$.

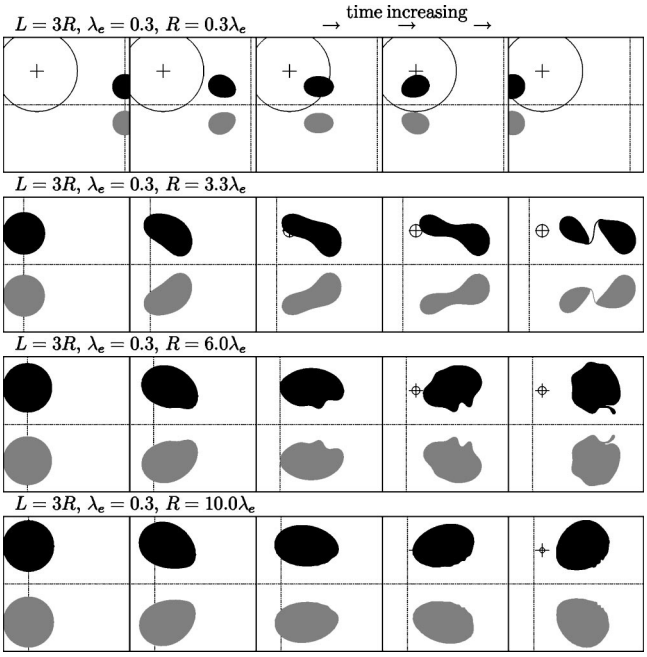

FIG. 19. Motion of a dipole, consisting of two circular ω_+ patches of opposite strength. Note that in the top row the dipole moves to the left whereas in the other cases it moves to the right.

C. Patches of opposite strength: Current-vortex dipoles

Finally, we consider a system of two patches with opposite strength, so $\omega_\pm = 1$ inside one and $\omega_\pm = -1$ inside the other patch. The motion for a dipole of two ω_+ patches is given in Figs. 19 and 20. A dipole vortex moves along the line perpendicular to the line between the two patches. The direction of this motion is determined by the sign of the interaction between the two patches. The small equal-type dipole therefore moves in the opposite direction compared to the larger ones, because $G \sim (1-\lambda_e^{-2})\ln r$ with $\lambda_e^{-2} > 1$ at small distances and $G \sim \ln r$ when $r \gg \lambda_e$. Again we see that the deformation of the patches causes them to break up into smaller parts. This deformation is less strong than in the case of vortices of like-sign strength, in particular when $R \gg \lambda_e$, because the shearing flow that the vortices impose on each other is less strong due to the larger mutual distance.

The case with $R = 3.3\lambda_e$ is given in Fig. 20 for longer times. A continuation of this run for even longer times eventually results in a vorticity distribution that increasingly lacks the symmetry with respect to the x axis, which is so characteristic in Figs. 19 and 20. As before these asymmetries are attributed to numerical errors that eventually invalidate the computational run.

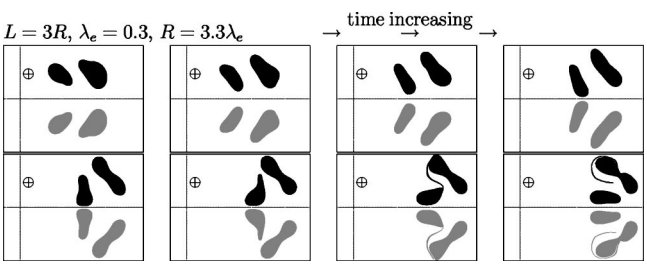

FIG. 20. Motion of a dipole, consisting of two circular ω_+ patches of opposite strength for $L = 3R$, $\lambda_e = 0.3$, $R = 3.3\lambda_e$.

In the case of a mixed-type dipole we see that patches of unequal type can indeed overlap. In this case thin ($\ll \lambda_e$) strands are pulled from the patches. Because the currents of the patches are in the same direction and thus attract each other at short distances, this overlapping motion can occur. This is in contrast with the motion of the mixed-type vortex pair (see preceding section, Fig. 17, where the currents repel each other and therefore prevent the patches from overlapping). In general the evolution of mixed-type dipoles show similar behavior as the equal-type dipole simulations do.

In conclusion we can say that in the interacting motion of two patches there is a tendency to form structures with a preferred size of a few Bessel scale lengths. Smaller vortices merge into larger ones, and larger vortices split up into structures of this preferred size. This preferred size is a result of the extremum in the interaction potential $G_{\alpha\beta}$. The splitting is initiated by a deformation of the patch due to other vortices, but it is in principle an internal process of the vorticity patch.

VI. CONCLUSIONS

In this paper we have presented a Contour Dynamics model for the Lagrangian three field drift-Alfvén model for a high temperature, strongly magnetized plasma. This method calculates the ideal dynamics of piecewise uniform distributions of the generalized vorticity fields. The dynamics of simple vortex patches has been studied numerically, as a paradigm for the interaction of separated vortical structures in a turbulent plasma or fluid. A contour surgery module has been added in order to follow the evolution of patches on a longer time scale.

The interaction potential between infinitesimal elements of vorticity consists of a logarithmic and a Bessel contribution. The first contribution represents Euler aspects of the interaction. The latter term is also a logarithm on short distances, but is shielded on long distances. In the interaction between elements of equal vorticity, the interaction potential has a minimum which introduces the length scale d_e into the problem. When d_e is smaller than the ion sound gyroradius ρ_s, the velocities induced between patches of equal vorticity have opposite directions on large and small mutual distances.

This scale d_e turns out to be a preferred size for structures that are formed in the interaction dynamics of patches. Quasiperiodic splitting-merging cycles of a single patch and in the interaction between vorticity patches have been observed numerically in runs of our Contour Dynamics code supplemented with a contour surgery module. Similar phenomena occur in more complex situations such as in the interaction between current filaments.[8] This generation of finite structures might also be closely related with the existence of different directions of turbulent cascades in wave number regions larger and smaller than d_e^{-1}. These phenomena disappear in the limits $d_e \to 0$ and $d_e \to \rho_s$. This regime where structures of size $O(d_e)$ are generated seems to differ from the one with ρ_s being smaller than or about equal to d_e.

This latter regime has been investigated in Refs. 18,19 in the case of the nonlinear evolution of a collisionless reconnection instability, where phase mixing of the Lagrangian invariants $\omega_\pm$ inside the magnetic islands is observed on small scales.

ACKNOWLEDGMENTS

The authors would like to thank Dr. P. W. C. Vosbeek for the provision of a Contour Dynamics algorithm and a contour surgery module that were modified to perform the calculations presented here. Fruitful discussions with Dr. F. Califano, Dr. F. Pegoraro, and Dr. R. R. Trieling are gratefully acknowledged.

This work was performed under the Euratom-FOM Association Agreement. The content of this publication is the sole responsibility of the publisher(s) and it does not necessarily represent the views of the Commission or its services.

APPENDIX A: THE DRIFT-ALFVÉN MODEL

The equations of motion of an electron guiding center in the fields (3) and (4) are given by

$$\frac{d\mathbf{x}}{dt} = \frac{c}{B_0}\mathbf{e}_z \times \boldsymbol{\nabla}\phi + v_z \mathbf{e}_z \times \boldsymbol{\nabla}\psi + v_z \mathbf{e}_z \tag{A1}$$

and

$$\frac{dv_z}{dt} = -\Omega_e \frac{\partial \Psi}{\partial t} + \frac{e}{m_e}\frac{\partial \phi}{\partial z} + \frac{e}{m_e}\mathbf{e}_z \times \boldsymbol{\nabla}\psi \cdot \boldsymbol{\nabla}\phi. \tag{A2}$$

The first term on the right of Eq. (A1) represents the electrostatic $\mathbf{E}\times\mathbf{B}$ drift and the remaining terms represent the particle motion along fluctuating field lines.

The associated drift-kinetic equation for the distribution function $f(\mathbf{x},t,v_z)$ is[20,21]

$$\frac{\partial f}{\partial t} + v_z\frac{\partial f}{\partial z} + v_z[\psi,f] + \frac{c}{B_0}[\phi,f] + \left\{-\Omega_e\frac{\partial \psi}{\partial t} + \frac{e}{m_e}\frac{\partial \phi}{\partial z} + \frac{e}{m_e}[\psi,\phi]\right\}\frac{\partial f}{\partial v_z} = 0, \tag{A3}$$

where the square brackets are defined by

$$[g,h] = \frac{\partial g}{\partial x}\frac{\partial h}{\partial y} - \frac{\partial g}{\partial y}\frac{\partial h}{\partial x}. \tag{A4}$$

In what follows we will limit the discussion to two-dimensional motion in the plane perpendicular to the strong field $\mathbf{B}_0$ and take all quantities to be independent of the coordinate z. As can easily be verified from Eqs. (A1) and (A2), the associated constant of the motion is the generalized momentum in the axial direction

$$V = v_z + \Omega_e \psi. \tag{A5}$$

Then, introducing the variables $(\mathbf{x},V,t)$ instead of $(\mathbf{x},v_z,t)$, the drift-kinetic equation for the distribution function $F(\mathbf{x},V,t)=f(\mathbf{x},t,v_z)$ can be written as

$$\frac{\partial F}{\partial t} + [W,F] = 0, \tag{A6}$$

where W is related with the particle energy

$$W = \frac{c}{B_0}\phi + V\psi - \frac{1}{2}\Omega_e\psi^2. \tag{A7}$$

The electron density is given by

$$n(\mathbf{r},t) = \int_{-\infty}^{+\infty} dv_z f = \int_{-\infty}^{+\infty} dV\, F. \tag{A8}$$

The electron current density j_z is related to the first moment of F according to

$$j_z(\mathbf{r},t) = -e\int_{-\infty}^{+\infty} dv_z v_z f = -e\int_{-\infty}^{+\infty} dV\, VF + en_e\Omega_e\psi. \tag{A9}$$

Since we will neglect the axial ion current, we may combine this expression with Ampere's law $j_z=(cB_0/4\pi)\nabla^2\psi$ to obtain

$$\nabla^2\psi - \frac{1}{d_e^2}\psi = -\frac{4\pi e}{cB_0}\int_{-\infty}^{+\infty} dV\, VF. \tag{A10}$$

Here, $d_e^2 = m_e c^2/4\pi n e^2$ is the electron inertial skin depth. We then integrate Eq. (A6) over V space and use Eq. (A10) to obtain

$$\frac{\partial n}{\partial t} + \frac{c}{B_0}[\phi,n] - \frac{cB_0}{4\pi e}[\psi,\nabla^2\psi] - \left[\frac{1}{2}\Omega_e\psi^2, n\right] = 0. \tag{A11}$$

Next, we multiply Eq. (A6) by V and integrate over V space. Thus it is found that

$$\frac{\partial}{\partial t}\left(\frac{\psi}{d_e^2} - \nabla^2\psi\right) + \frac{c}{B_0}\left[\phi, \frac{\psi}{d_e^2} - \nabla^2\psi\right] + \frac{4\pi e}{cB_0 m_e}[\psi, nT_e] - \Omega_e[\psi, \psi\nabla^2\psi] = 0, \tag{A12}$$

where $nT_e \equiv m_e\int v_z^2 f dv_z$. We break off the hierarchy of moment equations by assuming that the electron temperature T_e is constant throughout the plasma.

Finally, introducing the normalized quantities (6), the resulting expressions (A11) and (A12) can be conveniently written in the form,[7]

$$\frac{1}{\Omega_i}\frac{\partial \omega_\pm}{\partial t} + \rho_s^2[\Phi_\pm, \omega_\pm] - \rho_s^2\left[\frac{\Psi^2}{2\lambda_{e0}^2}, \omega_\mp\right] = 0, \tag{A13}$$

where

$$2\lambda_e\omega_\pm = \lambda_e N \pm d_{e0}^2\left(\frac{\Psi}{d_e^2} - \nabla^2\Psi\right) \tag{A14}$$

are generalized vorticities that are advected by the streaming potentials

$$\Phi_{\pm} = \Phi \pm \frac{1}{\lambda_e}\Psi. \tag{A15}$$

Here, $\rho_s^2 = T_e/m_i\Omega_i^2$ is the ion sound gyroradius and $\lambda_e = d_{e0}/\rho_s$, d_{e0} being the inertial skin depth at the reference density.

The first two terms of Eq. (A13) describe the Lagrangian advection of the generalized vorticities by the streaming potentials $\Phi_{\pm}$. The last term mixes ω_+ and ω_-. However, this term is one order higher in small quantities than the other terms and represents third-order nonlinearities. These will be neglected. In the same spirit, we will consider cases in which the electron density perturbations remain small such that n in d_e^2 may be replaced by its background value n_0.

The transverse ion motion consists of the $\mathbf{E}\times\mathbf{B}$ and the polarization drift

$$\mathbf{v}_{\perp i} = \frac{c}{B_0}\left\{\mathbf{e}_z \times \boldsymbol{\nabla}\phi - \frac{1}{\Omega_i}\left[\frac{\partial}{\partial t} + \frac{c}{B_0}(\mathbf{e}_z \times \boldsymbol{\nabla}\phi)\cdot\boldsymbol{\nabla}\right]\boldsymbol{\nabla}\phi\right\}. \tag{A16}$$

The axial ion motion is neglected. Substituting this expression into the ion continuity equation, invoking quasineutrality, leads to

$$\frac{1}{\Omega_i}\frac{\partial\omega_0}{\partial t} + \rho_s^2[\Phi,\omega_0] = 0, \tag{A17}$$

where

$$\omega_0 = \rho_s^2\nabla^2\Phi - N. \tag{A18}$$

APPENDIX B: CONTOUR DYNAMICS

Numerically, we solve the evolution in exactly the same way as described in Ref. 9, approximating the contours by a variable number of linear elements. The parametrization of the element between two nodes $\mathbf{x}_n = (x_n, y_n)$ and $\mathbf{x}_{n+1}$ is given by

$$\mathbf{x}_n(\xi) = \tfrac{1}{2}(1-\xi)\mathbf{x}_n + \tfrac{1}{2}(1+\xi)\mathbf{x}_{n+1}, \tag{B1}$$

where $-1 \leqslant \xi \leqslant 1$. The length of the element is denoted by h_n.

By fitting a quadratic polynomial through three consecutive points we can approximate the local curvature $\kappa = (x''y' - y''x')/(x'^2 + y'^2)^{3/2}$ (where a prime denotes derivation with respect to the parameter along the curve) at the node $\mathbf{x}_n$ by

$$\kappa_n = 8\frac{(x_{n+1}-x_n)(y_n-y_{n-1}) - (y_{n+1}-y_n)(x_n-x_{n-1})}{|\mathbf{x}_{n+1}-\mathbf{x}_{n-1}|^3}. \tag{B2}$$

Nodes are added and/or removed to meet the following criteria for all elements.

(1) Nodes are locally added to a contour if the curvatures at the nodes $\mathbf{x}_n$ and $\mathbf{x}_{n+1}$ become large, i.e., if

$$\delta_1 < \tfrac{1}{2}(|\kappa_n| + |\kappa_{n+1}|)h_n. \tag{B3}$$

(2) Locally a node is removed if the curvature at the nodes $\mathbf{x}_n$ and $\mathbf{x}_{n+1}$ becomes small, i.e., if

$$\tfrac{1}{2}(|\kappa_n| + |\kappa_{n+1}|)h_n < \delta_2, \tag{B4}$$

with $\delta_2 < \delta_1$.

(3) A node is removed if the local curvature at a certain point becomes smaller than a critical value.

(4) The nodes are distributed quasiuniformly:

$$\frac{h_{n-1}}{A} \leqslant h_n \leqslant Ah_{n-1}, \tag{B5}$$

where A is a constant larger than unity. (In practice $A \approx 2$.)

(5) The element length satisfies

$$h_{\min} < h_n < h_{\max}. \tag{B6}$$

(6) In order to keep track of the identity of contours, nodes are added to a contour at places where another contour (or another part of the same contour) approaches. When their mutual distance is below a certain critical distance and also when the ratio of their local curvatures becomes larger than a specified value, a node is added to the curve with the smallest curvature.

By tweaking the parameters $\delta_1, \delta_2, A, h_{\min}, h_{\max}$, and the critical distance between approaching features, one can ensure that the contours are approximated smoothly.

[1] J. C. McWilliams, J. Fluid Mech. **146**, 21 (1984).
[2] R. Benzi, S. Patarnello, and P. Santangelo, Europhys. Lett. **3**, 811 (1987).
[3] N. J. Zabusky, M. H. Hughes, and K. V. Roberts, J. Comput. Phys. **30**, 96 (1979), and references therein.
[4] P. W. C. Vosbeek, J. H. G. M. van Geffen, V. V. Meleshko, and G. J. F. van Heijst, Phys. Fluids **9**, 3315 (1997).
[5] V. P. Lakhin, T. J. Schep, and E. Westerhof, Phys. Plasmas **5**, 3833 (1998).
[6] D. G. Dritschel, Comput. Phys. Rep. **10**, 77 (1989).
[7] T. J. Schep, F. Pegoraro, and B. N. Kuvshinov, Phys. Plasmas **1**, 2843 (1994).
[8] J. Bergmans and T. J. Schep, Phys. Rev. Lett. **87**, 195002 (2001).
[9] P. W. C. Vosbeek and R. M. M. Matthheij, J. Comput. Phys. **133**, 222 (1997).
[10] P. W. C. Vosbeek (private communication).
[11] *FEMLAB Reference Manual, version 2.2* (COMSOL AB, Stockholm, Sweden, 2001).
[12] H. J. de Blank (private communication).
[13] P. G. Saffman, in *Vortex Dynamics* (Cambridge University Press, Cambridge, 1995), p. 167.
[14] H. Lamb, in *Hydrodynamics*, 6th ed. (Campridge University Press, New York, 1932), p. 232.
[15] A. E. H. Love, Proc. London Math. Soc. **35**, 18 (1893).
[16] D. N. Waugh, Phys. Fluids A **8**, 1745 (1992), and references therein.
[17] J. Bergmans, Ph.D. thesis, Eindhoven University of Technology, Eindhoven, 2001.
[18] D. Grasso, F. Califano, F. Pegoraro, and F. Porcelli, Phys. Rev. Lett. **86**, 5051 (2001).
[19] D. Del Sarto, F. Califano, and F. Pegoraro, Phys. Rev. Lett. **91**, 235001 (2003).
[20] D. Jovanović and F. Pegoraro, Phys. Rev. Lett. **84**, 95 (2000).
[21] H. J. de Blank, Phys. Plasmas **8**, 3927 (2001).